

# Resonant di-Higgs boson production in the $b\bar{b}WW$ channel: Probing the electroweak phase transition at the LHC

T. Huang,<sup>1,\*</sup> J. M. No,<sup>2,3,†</sup> L. Pernié,<sup>1,‡</sup> M. Ramsey-Musolf,<sup>4,5,§</sup> A. Safonov,<sup>1,||</sup> M. Spannowsky,<sup>1,¶</sup> and P. Winslow<sup>4,\*\*</sup>

<sup>1</sup>*Department of Physics and Astronomy, Texas A&M University, College Station, Texas 77843, USA*

<sup>2</sup>*Department of Physics, King's College London, Strand, WC2R 2LS London, United Kingdom*

<sup>3</sup>*Department of Physics and Astronomy, University of Sussex, Brighton BN1 9QH, United Kingdom*

<sup>4</sup>*Physics Department, University of Massachusetts Amherst, Amherst, Massachusetts 01003, USA*

<sup>5</sup>*Kellogg Radiation Laboratory, California Institute of Technology, Pasadena, California 91125, USA*

(Received 5 February 2017; published 11 August 2017)

We analyze the prospects for resonant di-Higgs production searches at the LHC in the  $b\bar{b}W^+W^-$  ( $W^+ \rightarrow \ell^+\nu_\ell$ ,  $W^- \rightarrow \ell^-\bar{\nu}_\ell$ ) channel, as a probe of the nature of the electroweak phase transition in Higgs portal extensions of the Standard Model. In order to maximize the sensitivity in this final state, we develop a new algorithm for the reconstruction of the  $b\bar{b}W^+W^-$  invariant mass in the presence of neutrinos from the  $W$  decays, building from a technique developed for the reconstruction of resonances decaying to  $\tau^+\tau^-$  pairs. We show that resonant di-Higgs production in the  $b\bar{b}W^+W^-$  channel could be a competitive probe of the electroweak phase transition already with the data sets to be collected by the CMS and ATLAS experiments in run 2 of the LHC. The increase in sensitivity with larger amounts of data accumulated during the high-luminosity LHC phase can be sufficient to enable a potential discovery of the resonant di-Higgs production in this channel.

DOI: [10.1103/PhysRevD.96.035007](https://doi.org/10.1103/PhysRevD.96.035007)

## I. MOTIVATION

With the discovery of the Higgs boson at the Large Hadron Collider (LHC) [1,2], exploring the thermal history associated with electroweak symmetry breaking (EWSB) has taken on heightened interest. In the Standard Model (SM), EWSB in the early Universe occurs through a crossover transition. In contrast, beyond-the-Standard-Model (BSM) scenarios may lead to a *bona fide* electroweak phase transition (EWPT). If such a transition occurred and was both first order and sufficiently strong, it could have provided the conditions needed for generating the observed cosmic matter-antimatter asymmetry.

Electroweak baryogenesis (EWBG) (for recent reviews, see Refs. [3,4]) is one of the most widely studied and experimentally testable scenarios for explaining the origin of the cosmic matter-antimatter asymmetry, characterized by the baryon-to-entropy density ratio  $Y_B = n_B/s$  as (most precisely) measured by Planck [5]:

$$Y_B = (8.59 \pm 0.11) \times 10^{-11}. \quad (1)$$

Successful baryogenesis requires three ingredients in the particle physics of the early Universe, the so-called

“Sakharov criteria” [6]: (i) baryon-number (B) violation, (ii) C and CP violation, and (iii) departure from thermal equilibrium or a breakdown of CPT invariance. The SM contains the requisite B violation in the guise of electroweak sphalerons, but it fails with regard to the last two criteria. CP violation in the SM, via the CKM mixing matrix, is too feeble. In the minimal SM, the maximum Higgs mass for a first-order EWPT is  $m_h \sim 70\text{--}80$  GeV, as confirmed by a variety of theoretical Monte Carlo simulations [7–11]; while for the observed  $m_h \sim 125$  GeV, EWSB occurred through a crossover phase transition in the early Universe, which would not provide for the necessary out-of-equilibrium conditions.

In contrast, if the observed Higgs boson resides within an extended scalar sector, the nature and properties of the EWPT could differ significantly from those of the SM. In that case, the Universe could have undergone a strong first-order EWPT even for a SM-like Higgs boson of mass  $m_h \sim 125$  GeV. The additional scalar degrees of freedom can alter the finite-temperature effective potential to make such a transition possible. The simplest realization of this possibility involves the extension of the SM Higgs sector by a single real scalar singlet  $S$ , the xSM [12–16]. While the xSM in and of itself is unlikely to be realized in nature, it embodies the phase transition dynamics associated with more complete models that contain a gauge singlet, such as the next-to-minimal supersymmetric Standard Model (NMSSM) [17,18], without introducing the complications associated with the other degrees of freedom present in these models. As such, it provides a framework for exploring generic features of singlet-driven phase transitions and the

\*taohuang@physics.tamu.edu

†jose\_miguel.no@kcl.ac.uk

‡lpernie@physics.tamu.edu

§mjrm@physics.umass.edu

||safonov@tamu.edu

¶michael.spannowsky@durham.ac.uk

\*\*pwinslow@physics.umass.edu

corresponding low-energy phenomenology. To enable a strong first-order EWPT in the xSM, the coupling(s) between the new scalar  $S$  and the SM Higgs doublet need to be sizable (though still perturbative). In general, the xSM gives rise to two neutral scalars  $h_{1,2}$  with masses  $m_{1,2}$  that are mixtures of the singlet and the neutral component of the doublet. The corresponding phenomenological consequences include reduced SM-like Higgs boson signal strengths [12,13,16], deviations of the trilinear Higgs self-coupling from its SM value [16,19], and resonant di-Higgs production [20,21].

In this work, we focus on resonant di-Higgs production at the LHC:  $pp \rightarrow h_2 \rightarrow h_1 h_1$ , where  $h_1$  ( $h_2$ ) denotes the SM-like (singlet-like) neutral scalars, for  $m_2 > 2m_1 = 250$  GeV. Within the SM, di-Higgs production is nonresonant, and search strategies have been proposed in  $b\bar{b}\gamma\gamma$  [22–26],  $b\bar{b}W^+W^-$  [27–29],  $b\bar{b}\tau^+\tau^-$  [27,30] and  $b\bar{b}b\bar{b}$  [31–33] final states, all found to be very challenging due to the smallness of the nonresonant di-Higgs cross section [34–38]. Hence, ongoing di-Higgs searches by ATLAS and CMS are looking beyond the SM paradigm, also focusing on resonance-enhanced production mechanisms [39–42].

In this context, two key issues need to be addressed. First, it is important to assess the LHC reach into the viable parameter space for a strong first-order EWPT. There have been initial studies in this context in the  $b\bar{b}\tau^+\tau^-$  final state [21], which found that discovery at the LHC may be possible with  $100 \text{ fb}^{-1}$  of integrated luminosity for relatively light  $h_2$  masses, but a comprehensive analysis has not yet been achieved. Second, in order to achieve maximal LHC sensitivity to the xSM, it is crucial to determine the degree to which different di-Higgs final states provide complementary probes of  $h_2$  in different regions of the possible  $m_2$  mass range. Here we consider the prospects for LHC discovery/exclusion of resonant di-Higgs production in the  $b\bar{b}W^+W^-$  channel, which has been initially studied in Ref. [43] for low- $m_2$  masses ( $m_2 < 500$  GeV). We cover the entire mass range  $250 \text{ GeV} < m_2 < 1 \text{ TeV}$ , focusing on what is possible to achieve with LHC run 2. We assess the LHC potential for probing the strong first-order EWPT parameter space by defining a set of 12 benchmark xSM parameter choices (corresponding to 12  $h_2$  mass windows in the range  $m_2 \in [250, 850]$  GeV), each of them giving the maximum resonant di-Higgs production cross section  $[(\sigma_{h_2} \times \text{BR}_{h_2 \rightarrow h_1 h_1})_{\text{max}}]$  consistent with a strong first-order EWPT within its mass window.

For the  $b\bar{b}W^+W^-$  analysis, we use a multivariate analysis (MVA) discriminator in order to efficiently discriminate the signal from  $t\bar{t}$  production, the most important SM background (particularly as  $m_2$  increases). Conventional experimental techniques do not allow full reconstruction of the resonance mass, which results in diminished discrimination against the leading background. To improve the sensitivity of the analysis, we have deployed a novel technique for the reconstruction of the

invariant mass  $m_2$  in the process  $h_2 \rightarrow h_1 h_1 \rightarrow b\bar{b}W^+W^-$  in the presence of neutrinos from the  $W$  decays. The proposed method builds on the missing mass calculator (MMC) technique developed for the reconstruction of resonances decaying to  $\tau^+\tau^-$  pairs [44]. The new technique provides an estimator for  $m_2$  using a likelihood constructed over the solutions of the kinematically underconstrained system and, for brevity, is referred to as the heavy mass estimator (HME) in the remainder of the paper.

We find that considering the  $\ell\nu\ell'\nu$  ( $\ell, \ell' = e, \mu$ ) final state (and assuming an eventual combination between the CMS and ATLAS experiments) allows us to probe into the strong first-order EWPT parameter space, defined by  $[(\sigma_{h_2} \times \text{BR}_{h_2 \rightarrow h_1 h_1})_{\text{max}}]$ , up to  $m_2 \sim 700$  GeV with  $300 \text{ fb}^{-1}$  of integrated luminosity, making this channel a promising avenue for analysis during LHC run 2 and the high-luminosity phase of the LHC (HL-LHC).

Our work is organized as follows: Sec. II gives an overview of the xSM, including a summary of current phenomenological constraints and the choice of first-order EWPT-viable benchmark points. In Sec. III, we discuss the analysis of the  $b\bar{b}WW$  channel in detail, including signal and background event generation, object reconstruction, and the algorithm for probabilistic reconstruction of the event kinematics. In Sec. IV, we apply this analysis to determine the LHC run 2 and HL-LHC reach. Finally, in Sec. V, we offer a summary and outlook.

## II. THE xSM

### A. The model

We consider the most general form for the xSM scalar potential that depends on a Higgs doublet,  $H$ , and real singlet,  $S$  (see e.g., Refs. [12–14]):

$$V(H, S) = -\mu^2(H^\dagger H) + \lambda(H^\dagger H)^2 + \frac{a_1}{2}(H^\dagger H)S + \frac{a_2}{2}(H^\dagger H)S^2 + \frac{b_2}{2}S^2 + \frac{b_3}{3}S^3 + \frac{b_4}{4}S^4. \quad (2)$$

The  $a_1$  and  $a_2$  parameters constitute the Higgs portal, providing the only connection between the SM and the singlet scalar  $S$ . We note that in the absence of  $a_1$  and the scalar self-interaction  $b_3$ , the potential (2) has a  $\mathbb{Z}_2$  symmetry that remains exact if the singlet field does not develop a vacuum expectation value (VEV). We, however, retain both parameters in the current study, as they play a leading role in the EWPT, as well as in di-Higgs production at colliders.

Boundedness of the scalar potential from below requires positivity of the quartic coefficients along all directions in field space. Along the  $h$  ( $s$ ) direction, this leads to the bound  $\lambda > 0$  ( $b_4 > 0$ ), while along an arbitrary direction this implies  $a_2 > -\sqrt{\lambda b_4}$ . After EWSB,  $H \rightarrow (v_0 + h)/\sqrt{2}$  with  $v_0 = 246$  GeV, and we allow for a possible VEV for

$S$ , i.e.  $S \rightarrow x_0 + s$ , where  $x_0$  is taken to be positive without any loss of generality (provided that  $a_1$  and  $b_3$  can take either sign).

The minimization conditions allow for two of the parameters in (2) to be expressed in terms of the VEVs and other parameters. For convenience, we choose

$$\begin{aligned} \mu^2 &= \lambda v_0^2 + (a_1 + a_2 x_0) \frac{x_0}{2}, \\ b_2 &= -b_3 x_0 - b_4 x_0^2 - \frac{a_1 v_0^2}{4x_0} - \frac{a_2 v_0^2}{2}. \end{aligned} \quad (3)$$

For viable EWSB, two conditions must be satisfied:  $(v_0, x_0)$  has to be a stable minimum, which requires

$$b_3 x_0 + 2b_4 x_0^2 - \frac{a_1 v_0^2}{4x_0} - \frac{(a_1 + 2a_2 x_0)^2}{8\lambda} > 0. \quad (4)$$

Furthermore, the electroweak minimum must be the absolute minimum, which we impose numerically. After EWSB, the Higgs portal parameters  $a_1$ ,  $a_2$  and the singlet VEV  $x_0$  induce a mixing between the states  $h$  and  $s$ . The mass-squared matrix entries are

$$\begin{aligned} m_h^2 &\equiv \frac{d^2 V}{dh^2} = 2\lambda v_0^2, \\ m_s^2 &\equiv \frac{d^2 V}{ds^2} = b_3 x_0 + 2b_4 x_0^2 - \frac{a_1 v_0^2}{4x_0}, \\ m_{hs}^2 &\equiv \frac{d^2 V}{dhds} = (a_1 + 2a_2 x_0) \frac{v_0}{2}, \end{aligned} \quad (5)$$

with the corresponding eigenvalues given by

$$m_{1,2}^2 = \frac{m_h^2 + m_s^2 \mp |m_h^2 - m_s^2| \sqrt{1 + \left(\frac{m_{hs}^2}{m_h^2 - m_s^2}\right)^2}}{2}, \quad (6)$$

with  $m_2 > m_1$  by construction. The mass eigenstates are given by

$$\begin{aligned} h_1 &= h \cos \theta + s \sin \theta, \\ h_2 &= -h \sin \theta + s \cos \theta, \end{aligned} \quad (7)$$

where we identify the more  $SU(2)_L$ -like state  $h_1$  with the Higgs boson observed at the LHC [1,2] by setting  $m_1 = 125$  GeV, and where  $h_2$  is a singlet-like mass eigenstate. The mixing angle  $\theta$  is defined as

$$\sin 2\theta = \frac{(a_1 + 2a_2 x_0)v_0}{(m_1^2 - m_2^2)}. \quad (8)$$

By virtue of (7), the couplings of  $h_1$  and  $h_2$  to SM vector bosons and fermions are universally rescaled with respect to the SM Higgs couplings:

$$g_{h_1 xx} = c_\theta g_{h xx}^{\text{SM}}, \quad g_{h_2 xx} = s_\theta g_{h xx}^{\text{SM}}, \quad (9)$$

with  $xx$  representing a SM final state different from  $xx = hh$ , and  $c_\theta, s_\theta \equiv \cos \theta, \sin \theta$ . In addition to these couplings, the triscalar interactions will play an important role in the following discussion of di-Higgs production. Of particular interest are the interactions  $\lambda_{211} h_2 h_1 h_1$  and  $\lambda_{111} h_1 h_1 h_1$ , which follow from (2) after EWSB, with

$$\begin{aligned} \lambda_{211} &= \frac{1}{4} [(a_1 + 2a_2 x_0) c_\theta^3 + 4v_0 (a_2 - 3\lambda) c_\theta^2 s_\theta \\ &\quad - 2(a_1 + 2a_2 x_0 - 2b_3 - 6b_4 x_0) c_\theta s_\theta^2 - 2a_2 v_0 s_\theta^3] \\ \lambda_{111} &= \lambda v_0 c_\theta^3 + \frac{1}{4} (a_1 + 2a_2 x_0) c_\theta^2 s_\theta + \frac{1}{2} a_2 v_0 c_\theta s_\theta^2 \\ &\quad + \left(\frac{b_3}{3} + b_4 x_0\right) s_\theta^3. \end{aligned} \quad (10)$$

## B. Current phenomenological constraints

The singlet-doublet mixing  $s_\theta$  is constrained by measurements of Higgs signal strengths, since all the signal rates associated with Higgs measurements get rescaled by  $c_\theta^2$ . Currently, the limit from LHC run 1 data is  $s_\theta^2 \leq 0.12$  at a 95% C.L. [45], while the projected 95% C.L. sensitivity for HL-LHC with  $3000 \text{ fb}^{-1}$  is  $s_\theta^2 \leq 0.063$  (assuming current theory uncertainties) [46].<sup>1</sup> In addition, ATLAS and CMS searches for a heavy SM-like Higgs boson provide a probe of  $h_2$ . For  $m_2 > 2m_1$ , which we focus on in this work, the decay mode  $h_2 \rightarrow h_1 h_1$  is kinematically allowed, with a partial width given by

$$\Gamma_{h_2 \rightarrow h_1 h_1} = \frac{\lambda_{211}^2 \sqrt{1 - 4m_1^2/m_2^2}}{8\pi m_2}. \quad (11)$$

Defining  $\Gamma^{\text{SM}}(m_2)$  as the SM Higgs width evaluated at  $m_2$  (as given, e.g., in Ref. [47]), the total width for the  $h_2$  boson is given by

$$\Gamma_{h_2} = s_\theta^2 \Gamma^{\text{SM}}(m_2) + \Gamma_{h_2 \rightarrow h_1 h_1}, \quad (12)$$

and the signal strength (normalized to the SM value for  $m_h = m_2$ ) for  $pp \rightarrow h_2 \rightarrow xx$  is

$$\mu_{h_2}^{xx} = s_\theta^4 \frac{\Gamma_{xx}^{\text{SM}}(m_2)}{\Gamma_{h_2}}. \quad (13)$$

<sup>1</sup>We note that measurements of  $c_\theta^2$  via Higgs signal strengths will have some sensitivity to the EWPT-viable parameter space, though it is not a one-to-one correspondence due to the presence of several parameters relevant to the phase transition strength. Delineating this complementarity will be the topic of a future study and goes beyond the scope of the present work, which focuses on resonant di-Higgs production.

By means of Eqs. (11)–(13), we can then express the production cross sections  $pp \rightarrow h_2 \rightarrow VV$  (with  $V = W, Z$  gauge bosons) and  $pp \rightarrow h_2 \rightarrow h_1 h_1$  as

$$\sigma_{VV} = \sigma^{\text{SM}}(m_2) \times s_\theta^4 \frac{\text{BR}_{VV}^{\text{SM}}(m_2)}{s_\theta^2 + \frac{\lambda_{211}^2}{v_0^2} f(m_2)}, \quad (14)$$

$$\sigma_{h_1 h_1} = \sigma^{\text{SM}}(m_2) \times s_\theta^2 \frac{\frac{\lambda_{211}^2}{v_0^2} f(m_2)}{s_\theta^2 + \frac{\lambda_{211}^2}{v_0^2} f(m_2)}, \quad (15)$$

with  $\sigma^{\text{SM}}(m_2)$  being the SM Higgs LHC production cross section and  $\text{BR}_{VV}^{\text{SM}}(m_2)$  the SM Higgs branching fraction into  $VV$  for  $m_h = m_2$ , and  $f(m_2)$  given by

$$f(m_2) = \frac{v_0^2 \sqrt{1 - 4m_1^2/m_2^2}}{8\pi m_2 \Gamma^{\text{SM}}(m_2)}. \quad (16)$$

We note that heavy Higgs searches in other final states (e.g.,  $h_2 \rightarrow \bar{f}f$ ) are much more challenging than the ones discussed above, and are disregarded in what follows. The ATLAS and CMS collaborations have performed searches for heavy Higgs bosons both in the  $h_2 \rightarrow VV$  [48–51] and in the  $h_2 \rightarrow h_1 h_1$  with  $h_1 h_1 \rightarrow b\bar{b}b\bar{b}$  [39,40] and  $h_1 h_1 \rightarrow b\bar{b}\gamma\gamma$ ,  $h_1 h_1 \rightarrow b\bar{b}\tau\tau$  [41,42]. In Fig. 1 we show the 95% C.L. limits from these searches in the  $(m_2, c_\theta)$  plane for increasing values of  $\lambda_{211}/v_0$ , using (15).

It is important to note that the limits shown in Fig. 1 are derived from present, publicly available (published) analyses, and better analysis techniques can make the  $h_2 \rightarrow h_1 h_1$  search channel much more sensitive, being highly complementary to the  $h_2 \rightarrow ZZ$  one. In this sense, we also stress that a discovery in any one channel would not by itself allow us to individually measure  $c_\theta$  and  $\lambda_{211}/v_0$ . This highlights the need to explore various channels and final states, like  $b\bar{b}WW$ , to correctly interpret a potential discovery of a new state  $h_2$ .

We now turn to the discussion of the constraints on  $m_2$  and  $c_\theta$  from electroweak precision observables (EWPO). The effects of the xSM on EWPO may be accurately characterized by its modification of the oblique parameters  $S, T$ , and  $U$  with respect to the SM. From (7), the shift in an oblique parameter  $\mathcal{O}$  can be written entirely in terms of the SM Higgs contribution to that parameter,  $\mathcal{O}^{\text{SM}}(m)$  (which can be found, e.g., in Refs. [52,53]), where  $m$  is either  $m_1$  or  $m_2$ . These shifts then take the form

$$\begin{aligned} \Delta\mathcal{O} &= (c_\theta^2 - 1)\mathcal{O}^{\text{SM}}(m_1) + s_\theta^2\mathcal{O}^{\text{SM}}(m_2) \\ &= s_\theta^2[\mathcal{O}^{\text{SM}}(m_2) - \mathcal{O}^{\text{SM}}(m_1)]. \end{aligned} \quad (17)$$

The best-fit values for the shifts  $\Delta\mathcal{O}_i^0$  and standard deviations  $\sigma_i$  from the most recent post-Higgs-discovery electroweak fit to the SM by the Gfitter group [54] (for

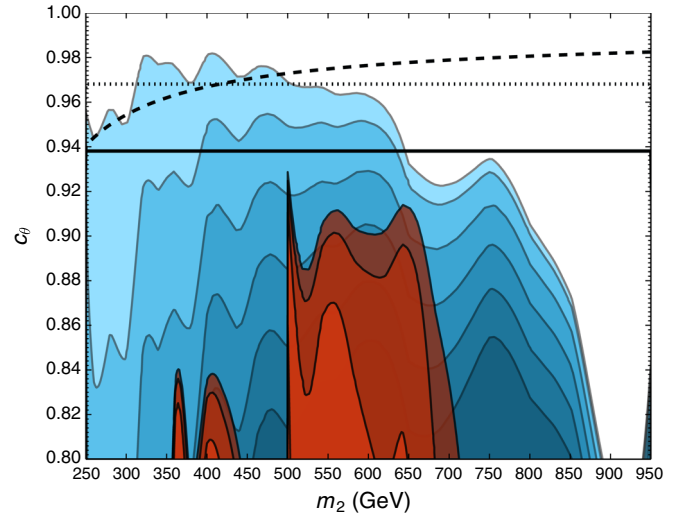


FIG. 1. Present 95% C.L. excluded regions from public ATLAS and CMS  $pp \rightarrow h_2 \rightarrow ZZ$  (blue) [48–51] and  $pp \rightarrow h_2 \rightarrow h_1 h_1$  (red) [39–42] searches in the  $(m_2, c_\theta)$  plane, for different values of  $\lambda_{211}/v_0$ . The color gradient for  $pp \rightarrow h_2 \rightarrow ZZ$  corresponds to values of  $\lambda_{211}/v_0 = 0, 1, 2, 3, 4, 5$  (from lighter to darker), while the color gradient for  $pp \rightarrow h_2 \rightarrow h_1 h_1$  corresponds to values of  $\lambda_{211}/v_0 = 3, 4, 5$  (from lighter to darker). Also shown are the present 95% C.L. lower limit on  $c_\theta$  from Higgs signal strength measurements (horizontal solid black line) [45] and the 95% C.L. lower limit on  $c_\theta(m_2)$  from EWPO (dashed black line), both being independent of  $\lambda_{211}/v_0$ . We also include the projected 95% C.L. lower limit on  $c_\theta$  from Higgs signal-strength measurements at HL-LHC with  $3000 \text{ fb}^{-1}$  (horizontal dotted black line) [46].

$U = 0$ , which is a very accurate approximation in the xSM) are given by

$$\begin{aligned} \Delta S &\equiv S - S_{\text{SM}} = 0.06 \pm 0.09, \\ \Delta T &\equiv T - T_{\text{SM}} = 0.10 \pm 0.07, \end{aligned} \quad (18)$$

$$\rho_{ij} = \begin{pmatrix} 1 & 0.91 \\ 0.91 & 1 \end{pmatrix}, \quad (19)$$

with  $\rho_{ij}$  being the covariance matrix in the  $(S, T)$  plane. We then perform a  $\Delta\chi^2$  fit to obtain the 95% C.L. allowed region in the  $(m_2, c_\theta)$  plane:

$$\begin{aligned} \Delta\chi_{\text{EW}}^2(m_2, c_\theta) &= \sum_{i,j} [\Delta\mathcal{O}_i(m_2, c_\theta) \\ &\quad - \Delta\mathcal{O}_i^0] (\sigma^2)_{ij}^{-1} (\Delta\mathcal{O}_j(m_2, c_\theta) - \Delta\mathcal{O}_j^0), \end{aligned} \quad (20)$$

where  $\Delta\mathcal{O}_i^0$  denote the central values in (18) and  $(\sigma^2)_{ij} \equiv \sigma_i \rho_{ij} \sigma_j$ , with  $\sigma_i$  being the  $S$  and  $T$  standard deviation from (18). The 95% C.L. exclusion limit from  $\Delta\chi_{\text{EW}}^2(m_2, c_\theta) = 5.99$  is shown in Fig. 1.

TABLE I. Values of the various xSM independent and dependent parameters for each of the benchmark values chosen to *maximize* the  $\sigma_{h_2} \times \text{BR}_{h_2 \rightarrow h_1 h_1}$  value at the LHC.

	$\cos \theta$	$m_2$ (GeV)	$\Gamma_{h_2}$ (GeV)	$x_0$ (GeV)	$\lambda$	$a_1$ (GeV)	$a_2$	$b_3$ (GeV)	$b_4$	$\lambda_{111}$ (GeV)	$\lambda_{211}$ (GeV)	$\sigma$ (pb)	BR
B1	0.961	258	0.68	307	0.52	-266	0.26	-138	0.26	110	-94.6	1.19	0.50
B2	0.976	341	2.42	257	0.92	-377	0.39	-403	0.77	204	-150	0.59	0.74
B3	0.982	353	2.17	265	0.99	-400	0.45	-378	0.69	226	-144	0.44	0.76
B4	0.983	415	1.59	54.6	0.17	-642	3.80	-214	0.16	44.9	82.5	0.36	0.33
B5	0.984	455	2.08	47.4	0.18	-707	4.63	-607	0.85	46.7	93.5	0.26	0.31
B6	0.986	511	2.44	40.7	0.18	-744	5.17	-618	0.82	46.6	91.9	0.15	0.24
B7	0.988	563	2.92	40.5	0.19	-844	5.85	-151	0.08	47.1	104	0.087	0.23
B8	0.992	604	2.82	36.4	0.18	-898	7.36	-424	0.28	45.6	119	0.045	0.30
B9	0.994	662	2.97	32.9	0.17	-976	8.98	-542	0.53	44.9	132	0.023	0.33
B10	0.993	714	3.27	29.2	0.18	-941	8.28	497	0.38	44.7	112	0.017	0.20
B11	0.996	767	2.83	24.5	0.17	-920	9.87	575	0.41	42.2	114	0.0082	0.22
B12	0.994	840	4.03	21.7	0.19	-988	9.22	356	0.83	43.9	83.8	0.0068	0.079

### C. The electroweak phase transition: Benchmarks for $h_2 \rightarrow h_1 h_1$ production

The character of the EWPT is understood in terms of the finite-temperature effective potential,  $V_{\text{eff}}^{T \neq 0}$  (see Ref. [55] for a review). It is well known that the standard derivation of  $V_{\text{eff}}^{T \neq 0}$  suffers from gauge dependence [56],<sup>2</sup> and here we employ a high-temperature expansion to restore gauge independence to our analysis (see Ref. [16] for details). Doing so requires considering the  $T = 0$  Coleman-Weinberg one-loop effective potential and retaining only the gauge-independent thermal mass corrections to  $V_{\text{eff}}^{T \neq 0}$ , which are essential for high-temperature electroweak symmetry restoration. This limit is particularly well suited to the xSM, which generates the barrier between the broken and unbroken electroweak phases required for a first-order EWPT at tree-level via the parameters  $a_1$  and  $b_3$  in (2).

In the high-temperature limit, we follow Refs. [12,57] and write the  $T$ -dependent, gauge-independent (indicated by the presence of a bar) VEVs in a cylindrical coordinate representation as

$$\bar{v}(T)/\sqrt{2} = \bar{\phi} \cos \alpha(T), \quad \bar{x}(T) = \bar{\phi} \sin \alpha(T), \quad (21)$$

with  $\bar{v}(T = 0) = v_0$  and  $\bar{x}(T = 0) = x_0$ . The critical values  $\bar{\phi}(T_c)$  and  $\alpha(T_c)$  are determined by minimizing  $V_{\text{eff}}^{T \neq 0}(\phi, \alpha, T)$ , while  $T_c$  is defined as the temperature at which the broken and unbroken phases are degenerate:  $V_{\text{eff}}^{T \neq 0}(\phi, \alpha \neq \pi/2, T_c) = V_{\text{eff}}^{T \neq 0}(\phi, \alpha = \pi/2, T_c)$ . A strong

<sup>2</sup>The value of the EWSB VEV at the critical temperature,  $\phi(T_c)$ , is inherently gauge dependent, as it is not an observable. Furthermore, the standard method for extracting  $T_c$  also introduces a separate and spurious gauge dependence. The consequence is that the conventional criterion for avoiding baryon washout during a first-order EWPT (which defines a ‘‘strong’’ first-order EWPT),  $\phi(T_c)/T_c \gtrsim 1$ , inherits both sources.

first-order EWPT is defined by a sufficient quenching of the sphaleron transitions in the broken electroweak phase (see, e.g., Ref. [3] for details). The energy of the electroweak sphaleron is proportional to the  $SU(2)_L$ -breaking energy scale,  $\bar{v}(T)$ , and as such the approximate criterion for a strong first-order EWPT is then  $\cos \alpha(T_c) \bar{\phi}(T_c)/T_c \gtrsim 1$ .

With these considerations in mind, we implement the xSM in the high-temperature limit in COSMOTRANSITIONS [58] to obtain numerically all above quantities characterizing the EWPT and calculate the finite-temperature thermal tunneling rate into the electroweak phase; the latter must be sufficiently fast in order to preclude the possibility of the Universe becoming stuck in a false metastable phase. Taking  $a_1, b_3, x_0, b_4$  and  $\lambda$  as our independent parameters (the remaining two are fixed by the values of  $v_0$  and  $m_h$ ), we perform a MC scan of the xSM parameter space within the following ranges:

$$(a_1/\text{TeV}), (b_3/\text{TeV}) \in [-1, 1], b_4, \lambda, (x_0/\text{TeV}) \in [0, 1], \quad (22)$$

where the lower bounds on the quartic couplings  $b_4$  and  $\lambda$  ensure vacuum stability. With our choice of independent parameters,  $c_\theta, a_2$  and  $m_2$  are fixed by the parameters of the scan. We impose a naive perturbativity bound on the Higgs portal coupling  $a_2/2 \lesssim 5$  [15]. We require compatibility with the various experimental constraints discussed in Sec. II B, and demand a strong first-order EWPT as described above, together with a sufficient tunneling rate.

From the results of our scan, we define 12 consecutive  $h_2$  mass windows, each 50 GeV wide (starting from the  $h_1 h_1$  production threshold  $m_2 = 250$  GeV), which together span the range  $m_2 \in [250, 850]$  GeV. The upper bound  $m_2 = 850$  GeV is determined by the fact that the scan does not yield experimentally viable points compatible with a strong first-order EWPT above  $m_2 \sim 850$  GeV, even

TABLE II. Values of the various xSM independent and dependent parameters for each of the benchmark values chosen to *minimize* the  $\sigma_{h_2} \times \text{BR}_{h_2 \rightarrow h_1 h_1}$  value at the LHC.

	$\cos \theta$	$m_2$ (GeV)	$\Gamma_{h_2}$ (GeV)	$x_0$ (GeV)	$\lambda$	$a_1$ (GeV)	$a_2$	$b_3$ (GeV)	$b_4$	$\lambda_{111}$ (GeV)	$\lambda_{211}$ (GeV)	$\sigma$ (pb)	BR
B1	0.999	279	0.03	140	0.13	-714	2.45	-93.6	0.36	1.017	0.11	0.03	0.60
B2	0.999	342	0.04	105	0.12	-849	3.91	-106	0.29	1.011	0.08	0.01	0.72
B3	0.973	350	0.77	225	0.17	-638	0.98	-110	0.97	1.189	0.04	0.66	0.01
B4	0.983	418	1.32	234	0.18	-980	1.55	0.41	0.96	1.227	0.04	0.42	0.01
B5	0.997	463	0.08	56.8	0.12	-763	6.34	112	0.73	1.015	0.06	0.00	0.62
B6	0.999	545	0.27	50.2	0.13	-948	8.64	151	0.56	1.039	0.08	0.00	0.62
B7	0.985	596	3.58	36.1	0.21	-760	4.02	676	0.69	1.454	0.07	0.08	0.04
B8	0.984	608	4.02	34.2	0.22	-821	4.53	-183	0.56	1.507	0.06	0.08	0.03
B9	0.986	698	5.10	29.7	0.23	-918	5.00	208	0.27	1.486	0.03	0.03	0.01
B10	0.990	729	4.22	27.3	0.20	-908	6.15	603	0.93	1.439	0.05	0.02	0.04
B11	0.995	792	3.36	22.2	0.18	-935	9.46	-848	0.65	1.371	0.07	0.00	0.12
B12	0.994	840	3.95	22.2	0.19	-955	8.68	683	0.53	1.363	0.05	0.00	0.06

though it potentially accepts points up to  $m_2 = 1$  TeV. Among all viable model points within each  $h_2$  mass window, we select the points which yield the maximum and the minimum resonant di-Higgs production cross section  $[(\sigma_{h_2} \times \text{BR}_{h_2 \rightarrow h_1 h_1})_{\text{max}}]$  (depending essentially on the values of  $c_\theta$  and  $\lambda_{211}$ , as discussed in Sec. II B) to define 12 xSM strong first-order EWPT-motivated benchmarks. These benchmark point sets, which we refer to in the following as  $\text{BM}^{\text{max}}$  and  $\text{BM}^{\text{min}}$ , are presented in Tables I and II, respectively. Searches for resonant di-Higgs production in the  $b\bar{b}W^+W^-$  channel sensitive to this set of benchmarks will be capable of probing into the strong first-order EWPT region. In the remainder of the paper, we assess the LHC potential to probe such a strong first-order EWPT via resonant di-Higgs production in the  $b\bar{b}W^+W^-$  final state.

### III. RESONANT DI-HIGGS PRODUCTION: THE $b\bar{b}W^+W^-$ CHANNEL

As discussed above, in this work we explore the LHC sensitivity to resonant di-Higgs production in the  $b\bar{b}W^+W^-$  ( $W^+ \rightarrow \ell^+\nu_\ell$ ,  $W^- \rightarrow \ell^-\bar{\nu}_\ell$ ) final state. By exploiting the two largest branching ratios of the 125 GeV Higgs boson  $h_1$ , we can retain sensitivity to smaller production cross sections, i.e. larger  $m_2$ , and develop dedicated reconstruction approaches to suppress SM backgrounds. We require both  $W$  bosons to decay leptonically (with  $\ell = e, \mu$ ) to suppress the otherwise overwhelming background from QCD multi-jet production. The cancellation of momenta of two neutrinos in the  $h_1 \rightarrow WW^* \rightarrow \ell\ell'\nu_\ell\bar{\nu}_{\ell'}$  decay does not allow us to reconstruct the invariant mass of the heavy resonance, which substantially diminishes the LHC sensitivity to resonant di-Higgs production. To improve the sensitivity of the search, we develop a novel technique, called the heavy mass estimator, designed to estimate the most likely invariant mass of the heavy  $h_2$  state probabilistically. The

technique is conceptually similar to the missing mass calculator (MMC) algorithm, which has previously been applied successfully to the mass reconstruction of resonances decaying into  $\tau^+\tau^-$  pairs [44,59].

Throughout the remainder of the paper, we assume an LHC center-of-mass energy of 13 TeV and an integrated luminosity ranging between  $300 \text{ fb}^{-1}$  and  $3000 \text{ fb}^{-1}$ , expected to be collected between the end of LHC run 2 data taking (foreseen in 2022) and the end of the high-luminosity phase of LHC (foreseen in 2035), respectively.

#### A. Monte Carlo generation and object reconstruction

For each of the xSM benchmark points in Table I, we generate our signal  $pp \rightarrow h_1 h_1 \rightarrow b\bar{b}W^+W^-$  ( $W^+ \rightarrow \ell^+\nu_\ell$ ,  $W^- \rightarrow \ell^-\bar{\nu}_\ell$ ) using HERWIG++ [60]. The dominant SM background is top-pair ( $t\bar{t}$ ) production,<sup>3</sup> which has been simulated at next-to-leading-order (NLO) accuracy with POWHEG [61] and then subsequently processed with HERWIG++ for parton showering and hadronization to evaluate experimental sensitivity. For simplicity, we restrict our signal and background Monte Carlo generation to  $\ell = \mu$ , but the subsequent sensitivity analysis takes into account the would-be contributions from final states with two electrons and one electron and one muon, for which we expect very similar efficiencies.

To evaluate the sensitivity achievable with the LHC data in this channel, we use the CMS detector and performance parameters as a benchmark. Assuming similar performance of the CMS and ATLAS detectors, in the combination we double the luminosity delivered per experiment. The simulation of the CMS detector response is performed using DELPHES 3.3.0 [62] and the input card recommended

<sup>3</sup>Other potential (and largely subdominant) backgrounds such as Drell-Yan, diboson, and single-top can be disregarded, as briefly discussed in Sec. III C.

by CMS [62,63], with all reconstructed physical objects, such as tracks, calorimeter deposits, isolated muons, electrons, jets, and missing transverse energy  $\vec{E}_T$ , used in the data analysis. Multiple proton-proton collisions during the same bunch crossing (pileup) can have a strong impact on hadronic observables, particularly during the high-luminosity LHC runs, and we include in our reconstruction the effect of an average of 40 simultaneous proton-proton interactions. A particle-flow algorithm [62] has been successfully deployed in the CMS experiment and is implemented in DELPHES parametrically using the information from the tracking system and the calorimeters. The particle-flow method is designed to reconstruct individual particles arising from collision by combining information from relevant subdetectors, to improve the quality of particle identification and the performance of global event reconstruction. Muons are reconstructed within the detector acceptance  $|\eta_\ell| < 2.4$ . Reconstruction and isolation selections follow the CMS definitions developed for particle flow muons [64] and use the medium working points for both. Jets are reconstructed using the anti- $k_r$  jet algorithm [65] with cone size  $R = 0.4$  by clustering the particle-flow tracks and particle-flow towers, and we require  $|\eta_j| < 4.0$ . The jet area method [62] in DELPHES is applied in jet reconstruction to subtract the pileup contribution. The  $b$ -tagging efficiency and mis-identification rates are modeled using the DELPHES parametrization of the CSV algorithm [66]. Tagging efficiencies and the mistag rates correspond to about 70% and 1.5% for the medium working point and 85% and 10% for the loose working point, respectively. The total transverse energy of a single event is calculated as the 2D-vector sum of the transverse momentum of all particles reconstructed by the CMS particle-flow algorithm. The missing transverse energy is defined as the opposite of the total transverse energy, and it quantifies the transverse energy carried away from neutrinos.

### B. Invariant mass reconstruction for $h_2$ : Heavy mass estimator

The cancellation of momenta of the two or more undetected neutrinos in the final state does not allow the reconstruction of the invariant mass of the heavy scalar  $h_2$  (and similarly for one of the 125 GeV scalars  $h_1$ ) using experimentally measurable quantities. To improve the analysis sensitivity, the HME technique, a MMC-like probabilistic algorithm [44,59], can be efficiently implemented for the reconstruction of the mass of  $h_2$ . To illustrate the implementation of the HME algorithm, we start with an idealized detector, in which properties of all visible particles are perfectly measured, and the missing transverse energy is equal to the negative vector sum of all visible particles. The latter assumes that the missing transverse energy measurement is not affected by pileup.

We note that for the production process considered, both 125 GeV  $h_1$  states are on shell, whereas one of the two  $W$

bosons from the  $h_1$  decay is typically off shell (we use the label 1 for the on-shell  $W$ ,  $W_1 \rightarrow \mu_1 \nu_{\mu_1}$ ). With these simplified assumptions, the kinematics of the majority of the signal events satisfies the following:

$$\vec{E}_{Tx} = p_x(\nu_{\ell_1}) + p_x(\nu_{\ell_2}), \quad (23)$$

$$\vec{E}_{Ty} = p_y(\nu_{\ell_1}) + p_y(\nu_{\ell_2}), \quad (24)$$

$$\sqrt{p^2(\ell_1, \nu_{\ell_1})} = M_W, \quad (25)$$

$$20 \text{ GeV} < \sqrt{p^2(\ell_2, \nu_{\ell_2})} < 45 \text{ GeV}, \quad (26)$$

$$(p(\ell_1) + p(\ell_2) + p(\nu_{\ell_1}) + p(\nu_{\ell_2}))^2 = m_{h_1}^2, \quad (27)$$

$$(p(b_1) + p(b_2))^2 = m_{h_1}^2, \quad (28)$$

where  $m_{h_1} \equiv m_1 = 125 \text{ GeV}$ ,  $\vec{E}_{Tx}$ ,  $\vec{E}_{Ty}$  are the  $x$ - and  $y$ -components of the missing transverse energy  $\vec{E}_T$  vector,  $p$  represent the various momentum four-vectors, and  $p_x$ ,  $p_y$  are their  $x$ - and  $y$ -components. The momentum carried by each neutrino is described by three unknown momentum projections, leading to a total of five equations, one bound and six unknowns.

As seen from Eqs. (23)–(28), four constraints reduce the number of unknowns to two, which we choose as the pseudorapidity  $\eta_{\nu_1}$  and azimuthal angle  $\phi_{\nu_1}$  of one neutrino. Assigning random values to these two unknowns would then allow one to scan the parameter space of allowed solutions to build a procedure to integrate over the space of solutions consistent with the experimental measured quantities. We refer to a single generation of the two unknowns as an *iteration* if it respects the bound for the invariant mass of the off-shell  $W$  (or else such a single generation is discarded). Each iteration yields an estimator for the mass of  $h_2$ :

$$m_2 = (p(\ell_1) + p(\ell_2) + p(\nu_{\ell_1}) + p(\nu_{\ell_2}) + p(b_1) + p(b_2))^2. \quad (29)$$

Furthermore, as not all pairs of values of the unknowns  $\eta_{\nu_1}$  and  $\phi_{\nu_1}$  are equally likely, generating pairs of these values according to a suitably defined probability density function would increase frequency of the estimated mass  $m_2$  being close to the true value. Such a probability density function (PDF) can be obtained from a Monte Carlo simulation. For each event, we generate thousands of iterations according to the PDF for  $\eta_{\nu_1}$  and  $\phi_{\nu_1}$ , and for each iteration we store the calculated value of  $m_2$ , building a probability distribution function for  $m_2$ , which we refer to as the HME *global likelihood function*. In the full implementation of the algorithm, the values of  $m_{h_1}$  and  $M_W$  used in Eqs. (25)–(28) are generated according to Gaussian functions to account

for the width of Higgs and  $W$  bosons. The addition of these two *variables* effectively increases the dimensionality of the space in which the scan is performed to 4. The introduction of additional probability density functions to account for realistic resolutions of experimental measurements further increases the dimensionality of the space scanned. One of the most essential additions accounts for the  $b$ -jet energy mismeasurements which leads to the invariant mass of the two  $b$ -jets being on average lower than  $m_{h_1}$ . We compute and apply an energy correction extracted from the simulation for the leading  $b$ -jet, and use Eq. (28) to correct the energy of the subleading  $b$ -jet. This procedure simultaneously improves the missing transverse energy estimation used in Eqs. (23) and (24) that is finally smeared according to the detector resolution predicted by DELPHES. Figure 2 (left) provides an illustration of a typical HME global likelihood for a single event, which peaks near the true value of the heavy scalar mass  $m_2$ . In this analysis, we use the most probable mass from the likelihood as the estimator of the heavy Higgs mass  $m_2$ . Note that selecting the peak position of a single event global likelihood as the estimator is the simplest solution, which one could likely improve upon by utilizing more information on the shape of the likelihood or even using the entire distribution in the analysis. Figure 2 (right) shows the reconstructed  $m_2$  mass for various xSM benchmark scenarios described in Table I.

### C. Analysis selection

The experimental signature consists of two energetic leptons, two energetic  $b$ -tagged jets and significant missing transverse energy due to neutrinos. As discussed above, the dominant SM background process is  $t\bar{t}$ , with a very large production cross section (see, e.g., Ref. [67]). Other potential SM backgrounds are Drell-Yan, single-top, diboson and  $t\bar{t}V$  production [68], as well as production of the SM Higgs boson (decaying to  $WW$ ) in association with jets (e.g., in vector boson fusion). However, it has been shown in Ref. [43] (see also Ref. [68]) that basic selection criteria together with mild kinematic cuts on  $p_T(b\bar{b})$ ,  $p_T(\ell\ell)$  and the invariant mass of the  $b\bar{b}$  and dilepton systems yield all these other backgrounds to be negligible, while maintaining a high signal efficiency. We therefore can safely disregard them in the present work.

Initial event preselection is performed as follows: we require the presence of two muons<sup>4</sup> with opposite signs and  $p_T \geq 10$  GeV,  $|\eta| < 2.4$ ; if more than two muons are present in the event, the two oppositely charged muons with the largest transverse momentum are selected. In addition, at least two  $b$ -tagged jets with  $p_T > 30$  GeV and  $|\eta| < 2.5$  are required. At least one of the two  $b$ -jet candidates has to be  $b$ -tagged using the CSV algorithm at the medium working point, while the other jet is only required to

<sup>4</sup>We recall that we have restricted our analysis to muons, yet it will apply equally to  $\ell = e, \mu$ .

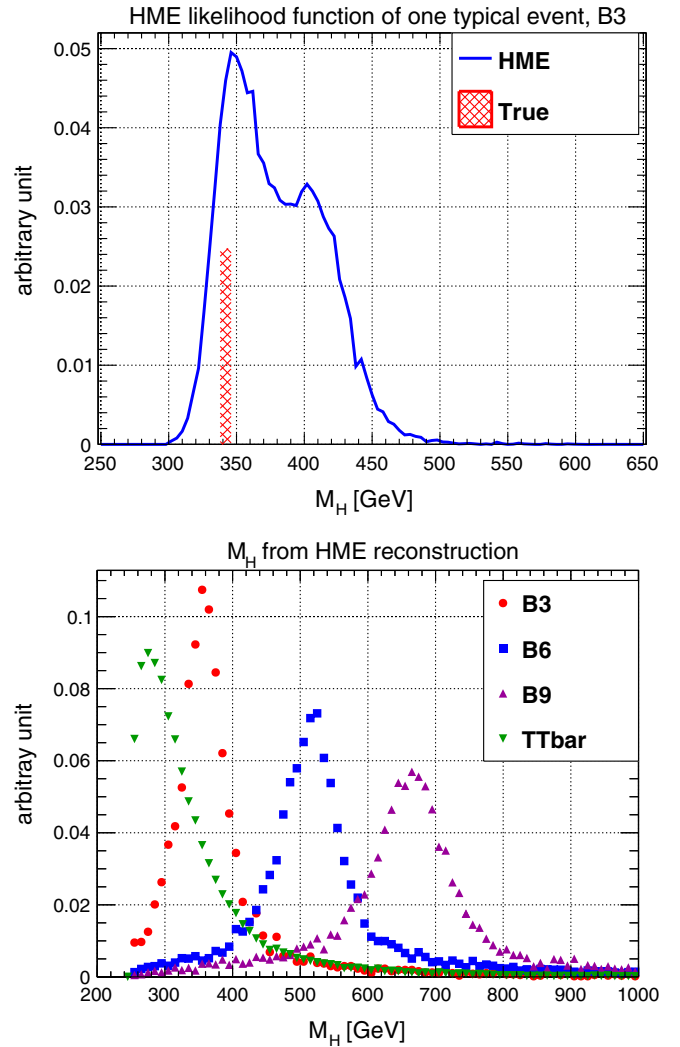


FIG. 2. Left: Global likelihood function (solid blue) computed from HME for a single signal event using the xSM benchmark point 3 (B3). The true value of the mass  $m_2$  is marked by the red grid bar. Right: HME distribution for B3 (red circle), B6 (blue square), B9 (magenta up triangle), and  $t\bar{t}$  (green down triangle). All distributions are normalized to unity.

satisfy at least the loose  $b$ -jet requirement. If more than two  $b$ -jets satisfy all selection criteria, the two  $b$ -jets candidates with the invariant mass closest to  $m_{h_1} = 125$  GeV are selected. Finally, we require the missing transverse energy to be  $E_T > 20$  GeV. After event preselection, we also perform a set of kinematic cuts (pre-MVA selection),

TABLE III. Pre-MVA selection.

Variable	Cut
$\Delta R(\ell\ell)$	$0.07 < \Delta R(\ell\ell) < 3.3$
$\Delta R(jj)$	$\Delta R(jj) < 5.0$
$m(\ell\ell)$	$5 \text{ GeV} < m(\ell\ell) < 100 \text{ GeV}$
$m(jj)$	$m(jj) > 22 \text{ GeV}$

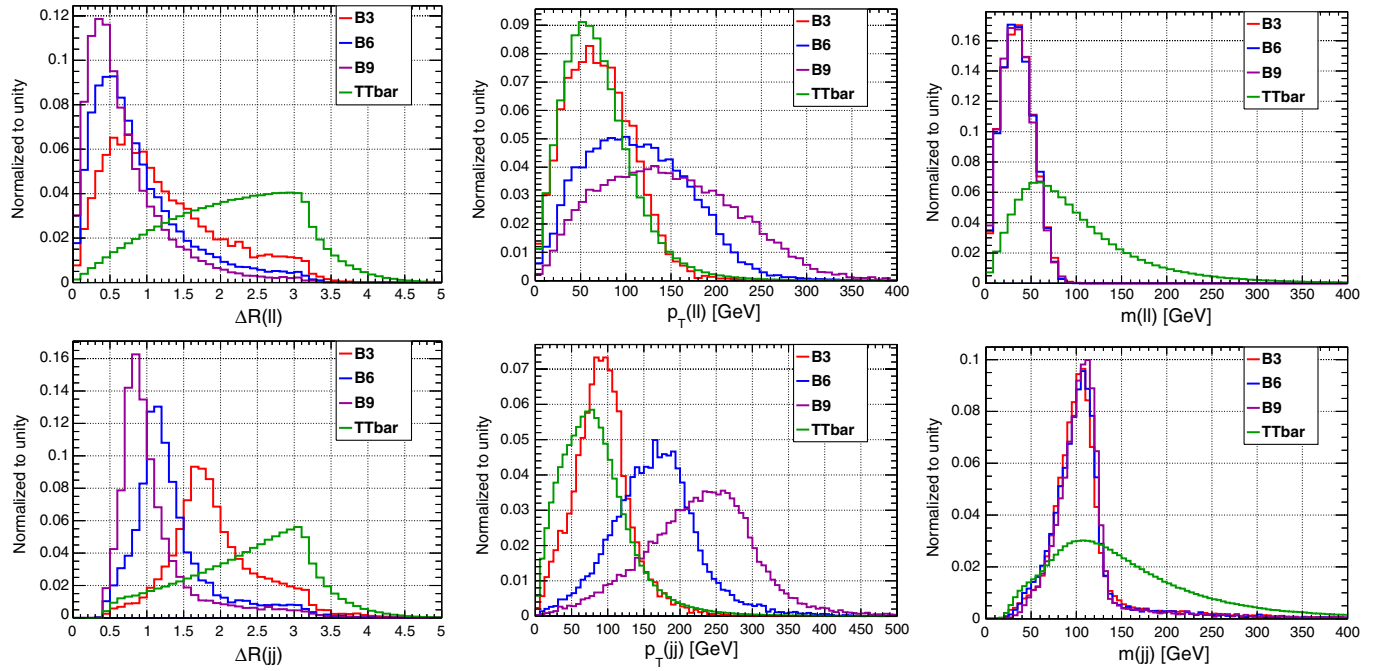


FIG. 3. Kinematic variables  $\Delta R(\ell\ell)$  (top left),  $p_T(\ell\ell)$  (top middle),  $m(\ell\ell)$  (top right),  $\Delta R(jj)$  (bottom left),  $p_T(jj)$  (bottom middle),  $m(jj)$  (bottom right), with distributions normalized to unity.

summarized in Table III, which reject approximately 5% of the signal events (for all signal mass points) and about 40% of  $t\bar{t}$  events.

In order to optimize the background and signal discrimination, we have tested several MVA algorithms (Likelihood, LikelihoodMIX, KNN, MLP, BDT, and BDTD) available from the TMVA package (version 4.1.2) [69], choosing the algorithm performing best in terms of background/signal discrimination as a function of  $m_2$ : a BDT for low mass (xSM benchmarks B1 to B7), and a Likelihood method for high mass (xSM benchmarks B8 to B12). The training of the MVA has been done independently for each signal mass point<sup>5</sup> considered in the analysis using the discriminating variables  $\Delta R(\ell\ell)$ ,  $p_T(\ell\ell)$ ,  $m(\ell\ell)$ ,  $\Delta R(jj)$ ,  $p_T(jj)$ ,  $m(jj)$ ,  $\Delta R(\ell, j)$ ,  $\Delta R(\ell\ell, jj)$ ,  $\Delta R_{\min}(\ell, j)$ ,  $\Delta\phi(\ell\ell, jj)$ ,  $m_T$  and  $m_{T2}$ . The variable  $\Delta R_{\min}(\ell, j)$  is computed by measuring the  $\Delta R$  between each lepton and each jet and selecting the smaller among these values. Kinematic distributions after preselection for the first six variables above are shown in Fig. 3 for the xSM signal samples B3, B6 and B9 together with the  $t\bar{t}$  background. The transverse mass variable  $m_T$  is defined as

$$m_T = \sqrt{2p_T(\ell\ell)\dot{E}_T[1 - \cos(\phi_{\ell\ell} - \phi_{\dot{E}_T})]}. \quad (30)$$

<sup>5</sup>The use of discrete mass values in this work is a simplification; in the actual data analysis, training of the MVA would be performed to optimize sensitivity within ranges of *target masses*  $m_2$ . Effectively, this would split the analysis into several sub-analyses, each optimized for a specific range of target masses  $m_2$ .

The  $m_{T2}$  variable [70,71] provides a transverse mass estimate in systems where more than one neutrino is present, treating the lepton and the  $b$ -jet as a single object. Figure 4 shows the  $m_T$  and  $m_{T2}$  distributions (normalized to unity) after the pre-MVA selection. The discriminating power of the  $m_{T2}$  variable in di-Higgs final states, already appreciated in Ref. [30], is good for all signal samples where the invariant mass of the heavy resonance is greater than twice the top mass.

Table IV shows the expected event yield  $N_{\text{event}}$  with  $300 \text{ fb}^{-1}$  of integrated luminosity for the  $t\bar{t}$  background and each of the xSM signal benchmarks after preselection and pre-MVA selection cuts, as well as the final yield of signal ( $N_S$ ) and background ( $N_B$ ) events after the MVA selection in each benchmark scenario. After the MVA-based selection is applied, the invariant mass of the heavy Higgs scalar  $h_2$  is reconstructed for the surviving events using the HME probabilistic technique described in Sec. III B. The HME distribution for signal and background is then used for setting upper limits on the signal production cross section.

#### D. Systematic uncertainties

For the systematic uncertainties in evaluating signal acceptance, we assume, based on previous publications presented by the CMS Collaboration, a conservative systematic uncertainty of about 10% [72–75]. This systematic includes the uncertainty on the integrated luminosity, the uncertainty on the trigger efficiency, the lepton identification and isolation, the uncertainty on the parton distribution functions (PDFs), and that on the factorization and renormalization scales.

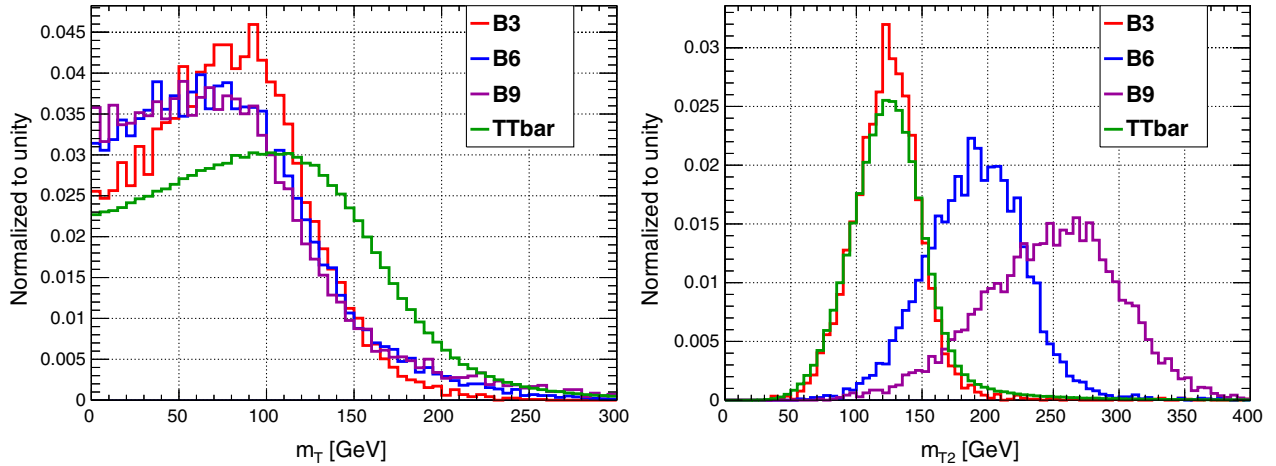


FIG. 4.  $m_T$  (left) and  $m_{T2}$  (right) distributions after the pre-MVA selection, with distributions normalized to unity.

The systematic uncertainties associated with the precision in the knowledge of the background shape and normalization can significantly affect the sensitivity of the analysis. In the absence of real data, we illustrate a possible way to estimate these uncertainties, which we believe to be conservative, as the experimentalists are likely to deploy more sophisticated approaches to reduce the impact of systematic uncertainty on the sensitivity, and we also anticipate improvements in the quality of the description of the  $t\bar{t}$  background arising from theoretical efforts and Monte Carlo tuning. For the purposes of this study, we define a control region dominated by the background, and use it to compare data and simulation to obtain a scale factor (SF) for correcting the simulation prediction for the  $t\bar{t}$  contribution. The control region is designed to contain background events with properties and kinematics as in the main signal region.

Since the  $t\bar{t}$  kinematics has no strong dependence on the dijet or dilepton invariant mass, we define control regions

TABLE IV. Number of signal ( $N_S$ ) and background ( $N_B$ ) events expected collecting  $300 \text{ fb}^{-1}$  of integrated luminosity after applying different stages of selection and prior to the final fit using the HME mass estimator distribution.

Process	$N_{\text{event}}$ (pre-selection)	$N_{\text{event}}$ (pre-MVA cuts)	$N_S$ (MVA)	$N_B$ (MVA)
B1	395	383	183	6962
B2	395	385	171	27372
B3	318	310	152	26593
B4	137	134	35	1425
B5	104	102	19	193
B6	52	50	12	95
B7	31	30	10	91
B8	22	21	4.5	28
B9	13	12	3.2	23
B10	5	5	1.2	13
B11	3	3	0.8	10
B12	1	1	0.2	4.5
$t\bar{t}$ Background	782721	382836		

by selecting events with the measured dijet invariant mass greater than 150 GeV or the dilepton invariant mass greater than 100 GeV (see Fig. 3). Using more than one control region allows us to cross-check and validate the scale factors and, if needed, adjust the uncertainty associated with the scale factors. Once the control region is defined, we apply the same kinematic selections and perform the MVA training exactly as it is done for the main analysis. We choose the MVA cut that yields the same background rejection as the cut that has been found to yield optimal sensitivity for the same target mass point in the main analysis. For all mass points, the signal contribution remains negligible in the control regions. Finally, the yield of surviving background events is used to derive the uncertainty in the scale factor (in our case, the same events play the role of both the “data” and the “prediction,” so the mean value of the scale factor is by definition equal to unity). Following this methodology, we estimate the systematic uncertainty on the knowledge of the background normalization to be 1% for the signal samples B1, B2 and B3; 5% for B4; 10% for B5; 12% for B6, B7, B8, B9, B10; and 15% for B11 and B12. In the final sensitivity estimates, for the three lowest mass points, we choose to increase the systematic uncertainty for the background normalization from 1% to 3%. This has been driven by the considerations that the lower-mass ranges are the most susceptible to the knowledge of the background normalization (this is because the EHM mass for  $t\bar{t}$  and the lower-mass signal samples are the most alike). Furthermore, the kinematic phase space of the control region never fully emulates the phase space of the signal region, and so actual data analyses are likely to use several control regions to ensure good control of the background normalization, which is likely to increase the systematic uncertainty.

#### IV. PROSPECTS FOR LHC RUN 2 AND HL-LHC

Once the full set of selections is applied to the signal and background samples, and the systematic uncertainties are

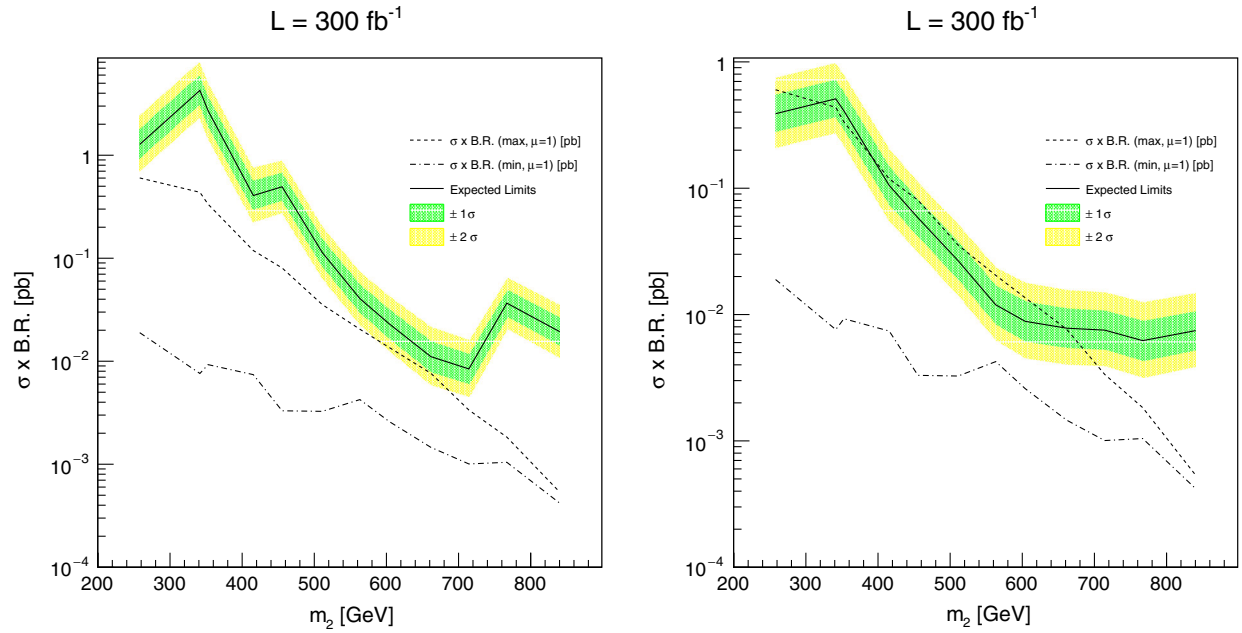


FIG. 5. The dashed (dash-dotted) lines represent the cross section times  $h_2 \rightarrow h_1 h_1$  branching ratio for each mass sample with  $\text{BM}^{\text{max}}$  ( $\text{BM}^{\text{min}}$ ). The continuous black line instead represents the predicted 95% C.L. upper limit on  $\sigma \times \text{BR}$  with  $300 \text{ fb}^{-1}$  of data collected. On the left, the limits are obtained by performing a cut-and-count experiment on the final number of signal and background events. The limit in this case is entirely driven by the high yield of the  $t\bar{t}$  background events, and the discontinuities are due to the noncontinuous assigned systematic uncertainty of the scale factors for the background normalization. The confidence intervals for the expected limit are given at 68% and 95% coverage probability. On the right, the limits are computed by fitting the HME distribution.

defined, we compute the expected limits on the resonant di-Higgs production cross section multiplied by the  $h_2 \rightarrow h_1 h_1$  branching fraction ( $\sigma \times \text{BR}$ ).

For calculations of expected limits, shown in Fig. 5, we adopt the modified frequentist criterion CLs [76]. The chosen test statistic, used to determine how signal- or background-like the data are, is based on the profile likelihood ratio [77]. Systematic uncertainties are incorporated in the analysis via nuisance parameters and are treated according to the frequentist paradigm. Results presented in this paper are obtained using asymptotic formulas [77]. The dashed lines represent the cross section times branching fraction expected for each mass point with  $\text{BM}^{\text{max}}$  and  $\text{BM}^{\text{min}}$ . Note that benchmark models are chosen as models yielding the highest ( $\text{BM}^{\text{max}}$ ) and lowest ( $\text{BM}^{\text{min}}$ ) cross sections for each mass range individually, which affects the smoothness of the theoretical prediction curve. The continuous black line represents the predicted 95% C.L. upper limit on the cross section times branching fraction  $\sigma_{h_2} \times \text{BR}_{h_2 \rightarrow h_1 h_1}$ . In Fig. 5 (left), the limits are shown using a cut-and-count analysis; i.e. applying the whole selection and counting the number of signal and background events expected at the end of the analysis. In this scenario, the heavy mass estimator developed in this study has not been used. This simplified method has substantially higher background contamination, with the limit being entirely driven by the background level. The discontinuity in the limit is an artifact of using noncontinuous systematic

uncertainties in the scale factors for background normalization (remember that the limits are calculated only for the discrete set of mass points connected by a line to guide the reader's eye). In Fig. 5 (right), the upper limits are computed by fitting the HME distribution, in which case the background under the signal peak is substantially lower and the use of the fit procedure reduces dependence on the background normalization scale factors. Limits are computed assuming a search with  $300 \text{ fb}^{-1}$  of integrated luminosity, using both electrons and muons in the final state, and presuming an eventual combination of the ATLAS and CMS data. Weakening of the limit at  $m_2 \sim 350 \text{ GeV}$  is due to the similarity of the HME shapes for the  $t\bar{t}$  background and signal in that mass range. Above  $m_2 \sim 600 \text{ GeV}$ , the limit trend changes. In this region, the number of  $t\bar{t}$  events in the signal region becomes almost constant, as can be seen in the  $t\bar{t}$  HME distribution in Fig. 2 (right), and the limit follows the same trend.

In Fig. 6, the limits are shown assuming  $3000 \text{ fb}^{-1}$  of integrated luminosity. We obtained such limits by scaling the number of events in the signal and background. We did not resimulate the pileup scenario. The local expected significance of the analysis is computed by generating toy models following the background hypothesis and the same profile likelihood ratio-based-CLs technique that has been used for deriving the limits. The local  $p$  value is then converted into significance  $\sigma$ , presented in Fig. 7. Both the limits and the sensitivity correspond to a combination of  $ee$ ,

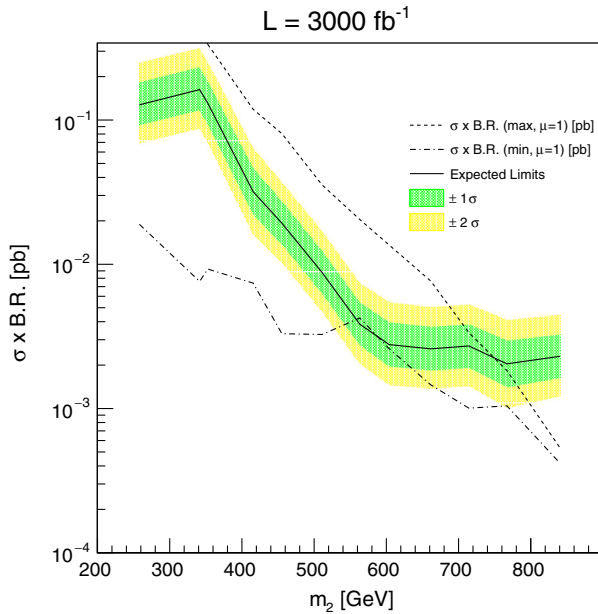


FIG. 6. The dashed (dash-dotted) lines represent the cross section times  $h_2 \rightarrow h_1 h_1$  branching ratio for each mass sample with  $\text{BM}^{\text{max}}$  ( $\text{BM}^{\text{min}}$ ). The continuous black line instead represents the  $\sigma \times \text{BR}$  excluded at 95% C.L. in the case where  $3000 \text{ fb}^{-1}$  of data are collected. The confidence intervals for the expected limit are given at 68% and 95% coverage probability.

$\mu\mu$  and  $e\mu$  channels with signal and background selection efficiencies equal to those for the  $\mu\mu$  channel studied in this paper, and an eventual combination of the CMS and ATLAS results. The sensitivity is shown assuming

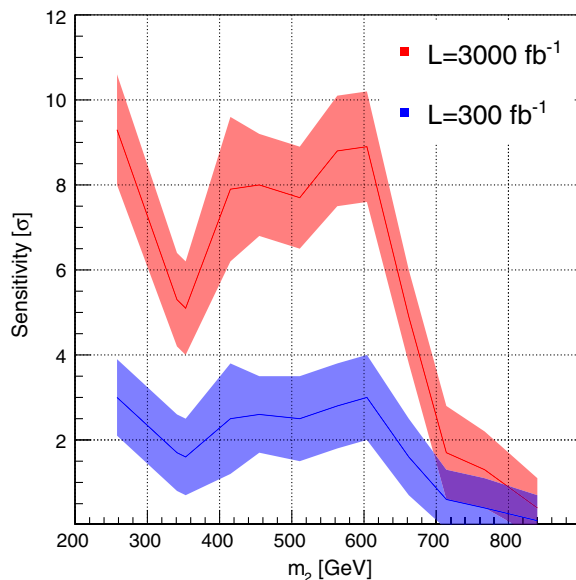


FIG. 7. The colored central lines represent the sensitivity of the analysis assuming  $300 \text{ fb}^{-1}$  of integrated luminosity (blue curve) and  $3000 \text{ fb}^{-1}$  (red curve). The confidence interval on the sensitivity central value is given at 68% coverage probability.

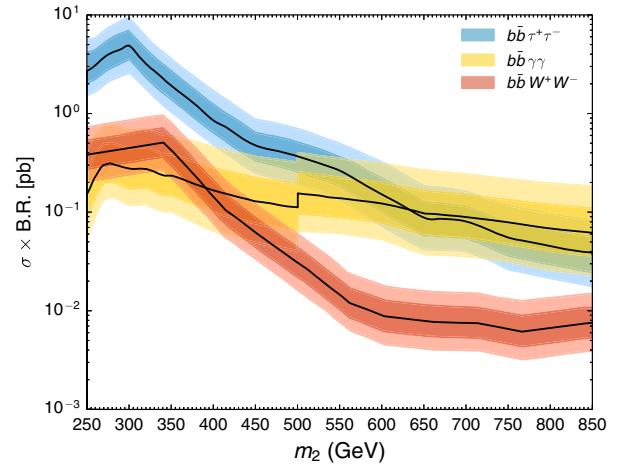


FIG. 8. 13 TeV LHC projected 95% C.L. limits (solid black lines) on  $\sigma_{pp \rightarrow h_2} \times \text{BR}_{h_2 \rightarrow h_1 h_1}$  (in pb) for an integrated luminosity  $\mathcal{L} = 300 \text{ fb}^{-1}$  and assuming an ATLAS-CMS combination, in the  $b\bar{b}W^+W^-$  final state [as shown in Fig. 5 (right)] and in the  $b\bar{b}\tau^+\tau^-$  and  $b\bar{b}\gamma\gamma$  final states (through a naive  $\sqrt{\mathcal{L}}$  extrapolation of the resonant di-Higgs 13 TeV CMS analysis in the  $b\bar{b}\tau^+\tau^-$  [78] and  $b\bar{b}\gamma\gamma$  [79] final states). In all cases, the dark (pale) colored bands correspond to the confidence intervals for the expected limit at 68% (95%) coverage probability.

$300 \text{ fb}^{-1}$  (blue curve) and  $3000 \text{ fb}^{-1}$  (red curve) of integrated luminosity per experiment. We find that  $3000 \text{ fb}^{-1}$  of data could allow for discovery for a significant portion of parameter space for  $m_2 \lesssim 700 \text{ GeV}$ . A possible exception is the region around  $m_2 = 350 \text{ GeV}$ , where fluctuations and the look-elsewhere effect may bring the global significance below the conventional  $5\sigma$  threshold. The confidence interval on the sensitivity central value is given at 68% coverage probability.

Finally, we compare the sensitivity of the  $b\bar{b}W^+W^-$  di-Higgs channel with those of the  $b\bar{b}\tau^+\tau^-$  and  $b\bar{b}\gamma\gamma$  channels. We extrapolate the current, public 13 TeV limits from the CMS search for resonant di-Higgs in  $b\bar{b}\tau^+\tau^-$  [78] and  $b\bar{b}\gamma\gamma$  [79] to  $300 \text{ fb}^{-1}$  of integrated luminosity, assuming a naive  $\sqrt{\mathcal{L}}$  (root-squared luminosity) improvement of the present CMS 95% C.L. limit in both final states, and compare it with the  $b\bar{b}W^+W^-$  limits from Fig. 5 (right).<sup>6</sup> The results are shown in Fig. 8, and they indicate that  $b\bar{b}\gamma\gamma$  provides the best limits for low- $h_2$  masses, while  $b\bar{b}W^+W^-$  may yield better limits than either  $b\bar{b}\gamma\gamma$  or  $b\bar{b}\tau^+\tau^-$  in the high-mass region. We nevertheless stress that this comparison of  $b\bar{b}\tau^+\tau^-$ ,  $b\bar{b}\gamma\gamma$  and  $b\bar{b}W^+W^-$  sensitivities is to be regarded

<sup>6</sup>We note that the results from Fig. 5 (right) assume an eventual combination of CMS and ATLAS. This means that a  $\sim\sqrt{2}$  sensitivity improvement should be added to the CMS  $b\bar{b}\tau^+\tau^-$  and  $b\bar{b}\gamma\gamma$  limits for a fair comparison. The comparison also assumes SM branching fractions for  $h_1$ , which is indeed the case for the xSM.

as only indicative, since it is expected that future sensitivity in the  $b\bar{b}\tau^+\tau^-$  and  $b\bar{b}\gamma\gamma$  final states will improve better than  $\sqrt{\mathcal{L}}$ , but a precise estimate of the comparative sensitivity is outside the scope of current work. Still, the comparison suggests that  $b\bar{b}W^+W^-$  is indeed a competitive search channel for resonant di-Higgs production at the LHC, particularly for high- $m_2$  masses.

## V. OUTLOOK

Exploring the thermal history of EWSB is an important endeavor for particle physics and one for which high-energy  $pp$  collisions at the LHC and future colliders can provide invaluable input. Monte Carlo studies imply that for the mass of the observed Higgs boson, EWSB in the SM occurs through a crossover transition. However, the simplest extension of the SM scalar sector—the xSM—may lead to a decidedly different thermal history. In particular, for suitable choices of model parameters, the xSM can generate a strong first-order EWPT, thereby fulfilling one of the key conditions for baryogenesis at the electroweak scale. Among the possible signatures of this possibility is resonant di-Higgs production in LHC  $pp$  collisions, catalyzed by the interaction of the singlet-like scalar with pairs of the SM-like Higgs bosons.

In order to fully probe this possibility, it is important to consider a variety of possible final states associated with the di-Higgs decay products. Here, we have considered the  $b\bar{b}W^+W^-$  channel, with the  $W$  bosons decaying leptonically. The presence of two neutrinos in the final state makes the reconstruction of the decaying Higgs-like boson (and thus, of the parent singlet-like scalar) challenging. To address this challenge, we have developed a new heavy mass estimator technique that allows one to achieve the needed mass reconstruction of the singlet-like scalar. Employing the HME and a MVA analysis of signal and background, we show that one is able to exclude the first-order EWPT parameter space associated with the maximum resonant di-Higgs production cross section with  $300\text{ fb}^{-1}$  of integrated luminosity for  $m_2 \lesssim 700\text{ GeV}$  and a statistically significant observation over roughly the same

mass range with  $3000\text{ fb}^{-1}$ . The projected sensitivity in the  $b\bar{b}W^+W^-$  channel exceeds in the high-mass region ( $m_2 \gtrsim 400\text{ GeV}$ ) expected from  $b\bar{b}\tau^+\tau^-$  and  $b\bar{b}\gamma\gamma$  channels based on a naive extrapolation of the present CMS 13 TeV public results for the latter channels, indicating that  $b\bar{b}W^+W^-$  is a competitive di-Higgs LHC search channel for high invariant masses.

Finally, putting our results in the context of other, prospective future collider probes, we note that part, but not all, of the EWPT-viable xSM parameter space accessible in the  $b\bar{b}W^+W^-$  channel at the LHC would be accessible with precision Higgs studies at the International Linear Collider with  $\sqrt{s} = 1\text{ TeV}$  and  $1\text{ ab}^{-1}$  integrated luminosity. Full access would require a circular  $e^+e^-$  collider ( $\sqrt{s} = 240\text{ GeV}$  and  $1\text{ ab}^{-1}$ ) [80]. Should the HL-LHC exclude this portion of parameter space, then a comprehensive probe would likely require a future 100 TeV  $pp$  collider.

## ACKNOWLEDGMENTS

We thank Andreas Papaefstathiou for support with HERWIG++. A. S. and T. H. are supported in part by U.S. Department of Energy Grant No. DE-SC0010813. A. S. and L. P. are supported in part by Qatar National Research Foundation Grant No. NPRP9-328-1-066. M. J. R. M. and P. W. are supported in part under U.S. Department of Energy Contract No. DE-SC0011095. J. M. N. is supported in part by the People Programme (Marie Curie Actions) of the European Union Seventh Framework Programme (No. FP7/2007-2013), by REA Grant Agreement No. PIEF-GA-2013-625809, and by the European Research Council under the European Unions Horizon 2020 program (ERC Grant Agreement No. 648680 DARKHORIZONS). J. M. N., M. J. R. M., M. S., and P. W. thank the Munich Institute for Astro- and Particle Physics (MIAPP), where a portion of this work has been completed. M. S. is supported in part by the European Commission through the ‘‘HiggsTools’’ Initial Training Network No. PITN-GA-2012-316704. Finally, we thank the CMS Collaboration for making DELPHES available.

- 
- [1] G. Aad *et al.* (ATLAS Collaboration), Observation of a new particle in the search for the Standard Model Higgs boson with the ATLAS detector at the LHC, *Phys. Lett. B* **716**, 1 (2012).  
 [2] S. Chatrchyan *et al.* (CMS Collaboration), Observation of a new boson at a mass of 125 GeV with the CMS experiment at the LHC, *Phys. Lett. B* **716**, 30 (2012).

- [3] D. E. Morrissey and M. J. Ramsey-Musolf, Electroweak baryogenesis, *New J. Phys.* **14**, 125003 (2012).  
 [4] T. Konstandin, Quantum transport and electroweak baryogenesis, *Phys. Usp.* **56**, 747 (2013).  
 [5] P. A. R. Ade *et al.* (Planck Collaboration), Planck 2013 results: XVI. Cosmological parameters, *Astron. Astrophys.* **571**, A16 (2014).

- [6] A. Sakharov, Violation of  $CP$  invariance,  $c$  asymmetry, and baryon asymmetry of the Universe, *Pis'ma Zh. Eksp. Teor. Fiz.* **5**, 32 (1967) [*JETP Lett.* **5**, 24 (1967)]; *Usp. Fiz. Nauk* **161**, 61 (1991) [*Sov. Phys. Usp.* **34**, 392 (1991)].
- [7] K. Kajantie, M. Laine, K. Rummukainen, and M. E. Shaposhnikov, Is There a Hot Electroweak Phase Transition at  $m(H)$  Larger or Equal to  $m(W)$ ? *Phys. Rev. Lett.* **77**, 2887 (1996).
- [8] M. Gurtler, E.-M. Ilgenfritz, and A. Schiller, Where the electroweak phase transition ends, *Phys. Rev. D* **56**, 3888 (1997).
- [9] M. Laine and K. Rummukainen, What's new with the electroweak phase transition?, *Nucl. Phys. B, Proc. Suppl.* **73**, 180 (1999).
- [10] F. Csikor, Z. Fodor, and J. Heitger, Endpoint of the Hot Electroweak Phase Transition, *Phys. Rev. Lett.* **82**, 21 (1999).
- [11] Y. Aoki, F. Csikor, Z. Fodor, and A. Ukawa, The endpoint of the first order phase transition of the  $SU(2)$  gauge Higgs model on a four-dimensional isotropic lattice, *Phys. Rev. D* **60**, 013001 (1999).
- [12] S. Profumo, M. J. Ramsey-Musolf, and G. Shaughnessy, Singlet Higgs phenomenology and the electroweak phase transition, *J. High Energy Phys.* **08** (2007) 010.
- [13] V. Barger, P. Langacker, M. McCaskey, M. J. Ramsey-Musolf, and G. Shaughnessy, LHC phenomenology of an extended Standard Model with a real scalar singlet, *Phys. Rev. D* **77**, 035005 (2008).
- [14] J. R. Espinosa, T. Konstandin, and F. Riva, Strong electroweak phase transitions in the Standard Model with a singlet, *Nucl. Phys.* **B854**, 592 (2012).
- [15] D. Curtin, P. Meade, and C.-T. Yu, Testing electroweak baryogenesis with future colliders, *J. High Energy Phys.* **11** (2014) 127.
- [16] S. Profumo, M. J. Ramsey-Musolf, C. L. Wainwright, and P. Winslow, Singlet-catalyzed electroweak phase transitions and precision Higgs boson studies, *Phys. Rev. D* **91**, 035018 (2015).
- [17] S. J. Huber, T. Konstandin, T. Prokopec, and M. G. Schmidt, Electroweak phase transition and baryogenesis in the nMSSM, *Nucl. Phys.* **B757**, 172 (2006).
- [18] J. Kozaczuk, S. Profumo, L. S. Haskins, and C. L. Wainwright, Cosmological phase transitions and their properties in the NMSSM, *J. High Energy Phys.* **01** (2015) 144.
- [19] A. Noble and M. Perelstein, Higgs self-coupling as a probe of electroweak phase transition, *Phys. Rev. D* **78**, 063518 (2008).
- [20] M. J. Dolan, C. Englert, and M. Spannowsky, New physics in LHC Higgs boson pair production, *Phys. Rev. D* **87**, 055002 (2013).
- [21] J. M. No and M. Ramsey-Musolf, Probing the Higgs portal at the LHC through resonant di-Higgs production, *Phys. Rev. D* **89**, 095031 (2014).
- [22] U. Baur, T. Plehn, and D. L. Rainwater, Determining the Higgs boson self-coupling at hadron colliders, *Phys. Rev. D* **67**, 033003 (2003).
- [23] U. Baur, T. Plehn, and D. L. Rainwater, Probing the Higgs self-coupling at hadron colliders using rare decays, *Phys. Rev. D* **69**, 053004 (2004).
- [24] N. Chen, C. Du, Y. Fang, and L.-C. Lü, LHC searches for the heavy Higgs boson via two  $b$  jets plus diphoton, *Phys. Rev. D* **89**, 115006 (2014).
- [25] A. Azatov, R. Contino, G. Panico, and M. Son, Effective field theory analysis of double Higgs boson production via gluon fusion, *Phys. Rev. D* **92**, 035001 (2015).
- [26] F. Kling, T. Plehn, and P. Schichtel, Mad-maximized Higgs pair analyses, *Phys. Rev. D* **95**, 035026 (2017).
- [27] M. J. Dolan, C. Englert, and M. Spannowsky, Higgs self-coupling measurements at the LHC, *J. High Energy Phys.* **10** (2012) 112.
- [28] A. Papaefstathiou, L. L. Yang, and J. Zurita, Higgs boson pair production at the LHC in the  $b\bar{b}W^+W^-$  channel, *Phys. Rev. D* **87**, 011301 (2013).
- [29] Z. Kang, J. Li, T. Li, D. Liu, and J. Shu, Probing the  $CP$ -even Higgs sector via  $H_3 H_2 H_1$  in the natural next-to-minimal supersymmetric Standard Model, *Phys. Rev. D* **88**, 015006 (2013).
- [30] A. J. Barr, M. J. Dolan, C. Englert, and M. Spannowsky, Di-Higgs final states augMT2ed—Selecting  $hh$  events at the high luminosity LHC, *Phys. Lett. B* **728**, 308 (2014).
- [31] D. E. Ferreira de Lima, A. Papaefstathiou, and M. Spannowsky, Standard Model Higgs boson pair production in the  $(b\bar{b})(b\bar{b})$  final state, *J. High Energy Phys.* **08** (2014) 030.
- [32] D. Wardrope, E. Jansen, N. Konstantinidis, B. Cooper, R. Falla, and N. Norjoharuddeen, Non-resonant Higgs-pair production in the  $b\bar{b} b\bar{b}$  final state at the LHC, *Eur. Phys. J. C* **75**, 219 (2015).
- [33] J. K. Behr, D. Bortoletto, J. A. Frost, N. P. Hartland, C. Issever, and J. Rojo, Boosting Higgs pair production in the  $b\bar{b}b\bar{b}$  final state with multivariate techniques, *Eur. Phys. J. C* **76**, 386 (2016).
- [34] J. Baglio, A. Djouadi, M. M. Grober, R. an Muhlleitner, J. Quevillon, and M. Spira, The measurement of the Higgs self-coupling at the LHC: Theoretical status, *J. High Energy Phys.* **04** (2013) 151.
- [35] D. de Florian and J. Mazzitelli, Higgs Boson Pair Production at Next-to-Next-to-Leading Order in QCD, *Phys. Rev. Lett.* **111**, 201801 (2013).
- [36] R. Frederix, S. Frixione, V. Hirschi, F. Maltoni, O. Mattelaer, P. Torrielli, E. Vryonidou, and M. Zaro, Higgs pair production at the LHC with NLO and parton-shower effects, *Phys. Lett. B* **732**, 142 (2014).
- [37] S. Borowka, N. Greiner, G. Heinrich, S. P. Jones, M. Kerner, J. Schlenk, U. Schubert, and T. Zirke, Higgs Boson Pair Production in Gluon Fusion at Next-to-Leading Order with Full Top-Quark Mass Dependence, *Phys. Rev. Lett.* **117**, 012001 (2016).
- [38] S. Borowka, N. Greiner, G. Heinrich, S. P. Jones, M. Kerner, J. Schlenk, and T. Zirke, Full top quark mass dependence in Higgs boson pair production at NLO, *J. High Energy Phys.* **10** (2016) 107.
- [39] M. Aaboud *et al.* (ATLAS Collaboration), Search for pair production of Higgs bosons in the  $b\bar{b}b\bar{b}$  final state using proton-proton collisions at  $\sqrt{s} = 13$  TeV with the ATLAS detector, *Phys. Rev. D* **94**, 052002 (2016).
- [40] V. Khachatryan *et al.* (CMS Collaboration), Search for heavy resonances decaying to two Higgs bosons in final

- states containing four  $b$  quarks, *Eur. Phys. J. C* **76**, 371 (2016).
- [41] V. Khachatryan *et al.* (CMS Collaboration), Search for two Higgs bosons in final states containing two photons and two bottom quarks in proton-proton collisions at 8 TeV, *Phys. Rev. D* **94**, 052012 (2016).
- [42] G. Aad *et al.* (ATLAS Collaboration), Searches for Higgs boson pair production in the  $hh \rightarrow bb\tau\tau, \gamma\gamma WW^*, \gamma\gamma bb, bbbb$  channels with the ATLAS detector, *Phys. Rev. D* **92**, 092004 (2015).
- [43] V. M. Lozano, J. M. Moreno, and C. B. Park, Resonant Higgs boson pair production in the  $hh \rightarrow bbWW \rightarrow bb\ell^+\nu\ell^-\bar{\nu}$  decay channel, *J. High Energy Phys.* **08** (2015) 004.
- [44] A. Elagin, P. Murat, A. Pranko, and A. Safonov, A new mass reconstruction technique for resonances decaying to di-tau, *Nucl. Instrum. Methods Phys. Res., Sect. A* **654**, 481 (2011).
- [45] G. Aad *et al.* (ATLAS Collaboration), Constraints on new phenomena via Higgs boson couplings and invisible decays with the ATLAS detector, *J. High Energy Phys.* **11** (2015) 206.
- [46] ATLAS Collaboration, ATLAS Report No. ATLAS-PHYS-PUB-2014-016, 2014.
- [47] J. R. Andersen *et al.* (LHC Higgs Cross Section Working Group Collaboration), Handbook of LHC Higgs cross sections: 3. Higgs properties, [arXiv:1307.1347](https://arxiv.org/abs/1307.1347).
- [48] G. Aad *et al.* (ATLAS Collaboration), Search for an additional, heavy Higgs boson in the  $H \rightarrow ZZ$  decay channel at  $\sqrt{s} = 8$  TeV in  $pp$  collision data with the ATLAS detector, *Eur. Phys. J. C* **76**, 45 (2016).
- [49] G. Aad *et al.* (ATLAS Collaboration), Combination of searches for  $WW, WZ$ , and  $ZZ$  resonances in  $pp$  collisions at  $\sqrt{s} = 8$  TeV with the ATLAS detector, *Phys. Lett. B* **755**, 285 (2016).
- [50] S. Chatrchyan *et al.* (CMS Collaboration), Search for a Standard-Model-like Higgs boson with a mass in the range 145 to 1000 GeV at the LHC, *Eur. Phys. J. C* **73**, 2469 (2013).
- [51] V. Khachatryan *et al.* (CMS Collaboration), Search for a Higgs boson in the mass range from 145 to 1000 GeV decaying to a pair of  $W$  or  $Z$  bosons, *J. High Energy Phys.* **10** (2015) 144.
- [52] M. E. Peskin and T. Takeuchi, Estimation of oblique electroweak corrections, *Phys. Rev. D* **46**, 381 (1992).
- [53] K. Hagiwara, S. Matsumoto, D. Haidt, and C. S. Kim, A novel approach to confront electroweak data and theory, *Z. Phys. C* **64**, 559 (1994).
- [54] M. Baak, J. Cúth, J. Haller, A. Hoecker, R. Kogler, K. Mönig, M. Schott, and J. Stelzer, The global electroweak fit at NNLO and prospects for the LHC and ILC, *Eur. Phys. J. C* **74**, 3046 (2014).
- [55] M. Quiros, Field theory at finite temperature and phase transitions, *Helv. Phys. Acta* **67**, 451 (1994).
- [56] H. H. Patel and M. J. Ramsey-Musolf, Baryon washout, electroweak phase transition, and perturbation theory, *J. High Energy Phys.* **07** (2011) 029.
- [57] M. Pietroni, The electroweak phase transition in a nonminimal supersymmetric model, *Nucl. Phys. B* **402**, 27 (1993).
- [58] C. L. Wainwright, CosmoTransitions: Computing cosmological phase transition temperatures and bubble profiles with multiple fields, *Comput. Phys. Commun.* **183**, 2006 (2012).
- [59] M. Spannowsky and C. Wymant, Making the most of missing transverse energy: Mass reconstruction from collimated decays, *Phys. Rev. D* **87**, 074004 (2013).
- [60] M. Bahr *et al.*, Herwig++ physics and manual, *Eur. Phys. J. C* **58**, 639 (2008).
- [61] S. Alioli, P. Nason, C. Oleari, and E. Re, A general framework for implementing NLO calculations in shower Monte Carlo programs: The POWHEG BOX, *J. High Energy Phys.* **06** (2010) 043.
- [62] J. de Favereau, C. Delaere, P. Demin, A. Giammanco, V. Lemaitre, A. Mertens, and M. Selvaggi, DELPHES 3: A modular framework for fast simulation of a generic collider experiment, *J. High Energy Phys.* **02** (2014) 057.
- [63] CMS Collaboration, CMS, the Compact Muon Solenoid: Technical proposal, CERN-LHCC-94-38, CERN-LHCC-P-1.
- [64] S. Chatrchyan *et al.* (CMS Collaboration), Performance of CMS muon reconstruction in  $pp$  collision events at  $\sqrt{s} = 7$  TeV, *J. Instrum.* **7**, P10002 (2012).
- [65] M. Cacciari, G. P. Salam, and G. Soyez, The anti- $k_t$  jet clustering algorithm, *J. High Energy Phys.* **04** (2008) 063.
- [66] S. Chatrchyan *et al.* (CMS Collaboration), Identification of  $b$ -quark jets with the CMS experiment, *J. Instrum.* **8**, P04013 (2013).
- [67] CMS Collaboration, CERN Technical Report No. CMS-PAS-TOP-15-010, 2015.
- [68] CMS Collaboration, Search for resonant Higgs boson pair production in the  $b\bar{b}\nu\nu$  final state at  $\sqrt{s} = 13$  TeV, CMS-PAS-HIG-16-011.
- [69] A. Hocker *et al.*, TMVA: Toolkit for multivariate data analysis, *Proc. Sci.*, ACAT2007 (2007) 040.
- [70] C. G. Lester and D. J. Summers, Measuring masses of semi-invisibly decaying particles pair produced at hadron colliders, *Phys. Lett. B* **463**, 99 (1999).
- [71] A. Barr, C. Lester, and P. Stephens,  $m_{T2}$ : The truth behind the glamour, *J. Phys. G* **29**, 2343 (2003).
- [72] CMS Collaboration, A search for pair production of new light bosons decaying into muons, *Phys. Lett. B* **752**, 146 (2016).
- [73] CMS Collaboration, Search for a light charged Higgs boson decaying to  $cs$  in  $pp$  collisions at  $\sqrt{s} = 8$  TeV, *J. High Energy Phys.* **12** (2015) 1.
- [74] CMS Collaboration, Search for two Higgs bosons in final states containing two photons and two bottom quarks, *Phys. Rev. D* **94**, 052012 (2016).
- [75] CMS Collaboration, Search for a low-mass pseudoscalar Higgs boson produced in association with a  $bb$  pair in  $pp$  collisions at  $\sqrt{s} = 8$  TeV, *Phys. Lett. B* **758**, 296 (2016).
- [76] A. L. Read, Presentation of search results: The  $CL_s$  technique, *J. Phys. G* **28**, 2693 (2002).
- [77] G. Cowan, K. Cranmer, E. Gross, and O. Vitells, Asymptotic formulae for likelihood-based tests of new physics, *Eur. Phys. J. C* **71**, 1554 (2011); Erratum, *Eur. Phys. J. C* **73**, 2501 (2013).
- [78] CMS Collaboration, CMS Public Analysis No. HIG-16-029, 2016.
- [79] CMS Collaboration, CMS Public Analysis No. HIG-16-032, 2016.
- [80] A. V. Kotwal, M. J. Ramsey-Musolf, J. M. No, and P. Winslow, Singlet-catalyzed electroweak phase transitions in the 100 TeV frontier, *Phys. Rev. D* **94**, 035022 (2016).